



| | |
|-------------------------------|---|
| Publication Year | 2017 |
| Acceptance in OA @INAF | 2021-02-25T15:17:02Z |
| Title | Signal-adapted tomography as a tool for dust devil detection |
| Authors | Aguirre, C.; Franzese, Gabriele; ESPOSITO, Francesca; Vázquez, Luis; Caro-Carretero, Raquel; et al. |
| DOI | 10.1016/j.aeolia.2017.09.005 |
| Handle | http://hdl.handle.net/20.500.12386/30618 |
| Journal | AEOLIAN RESEARCH |
| Number | 29 |

1
2
3 **Signal-adapted tomography as a tool for dust devil detection**
4
5
6

7 **ABSTRACT**
8

9 Dust devils are important phenomena to take into account to understand the global dust
10 circulation of a planet. On Earth, their contribution to the injection of dust into the atmosphere
11 seems to be secondary. Elsewhere, there are many indications that the dust devil's role on other
12 planets, in particular on Mars, could be fundamental, impacting the global climate. The ability
13 to identify and study these vortices from the acquired meteorological measurements assumes a
14 great importance for planetary science.

15 Here we present a new methodology to identify dust devils from the pressure time series testing
16 the method on the data acquired during a 2013 field campaign performed in the Tafilalt region
17 (Morocco) of the North-Western Sahara Desert. Although the analysis of pressure is usually
18 studied in the time domain, we prefer here to follow a different approach and perform the
19 analysis in a time signal-adapted domain, the relation between the two being a bilinear
20 transformation, i.e. a tomogram. The tomographic technique has already been successfully
21 applied in other research fields like those of plasma reflectometry or the neuronal signatures.
22 Here we show its effectiveness also in the dust devils detection. To test our results, we compare
23 the tomography with a phase picker time domain analysis. We show the level of agreement
24 between the two methodologies and the advantages and disadvantages of the tomographic
25 approach.
26

27 **KEYWORDS:** Mars; Dust devils; Tomography technique; Meteorology; North-Western Sahara
28
29

30 **1. INTRODUCTION**
31

32 Dust devils are dust loaded convective vortices, with diameters of a few meters and heights of
33 an order of magnitude larger. Their formation is favoured in conditions of strong insolation, low
34 humidity environment, lack of vegetation and buildings or other high obstacles and gently
35 sloping topography (Balme and Greeley, 2006). For these reasons, they are often observed in
36 terrestrial deserts and are also very common on the surface of Mars.

37 Martian and terrestrial dust devils have a common formation mechanism and similar dynamics
38 (Ringrose et al., 2003), but the Martian dust devils can be an order of magnitude larger than the
39 terrestrial ones (Fenton et al., 2016).

40 Dust devils are one of the most efficient aeolian mechanisms able to lift material from the
41 surface and inject dust into the atmosphere, through the combined effect of the vertical wind,
42 saltation process and pressure-gradient force (Balme et al., 2003; Klose et al., 2016).

43 The relative importance of the three mechanisms is still unclear, but, their sum makes the dust
44 devil a more effective dust lifting-phenomena compared to the common atmospheric boundary
45 layer winds (Greeley et al., 2003).

46 On Mars, the optimum size of the grains lifted by the boundary layer winds is around 100 μm
47 and the value of the friction velocity threshold grows rapidly for particles smaller and bigger
48 than this optimum size. However, the typical size of grains that compose the observed Martian
49 haze and the local and global dust storms is in the order of about 3 microns in diameter and even
50 smaller in some cases (Pollack et al., 1979). Due to the low Martian surface pressure, the
51 boundary layer wind required to mobilize such small grains exceeds the speed of sound (Iversen
52 and White, 1982) and is much faster than the typical winds observed or predicted from climate
53 models.

54 The small grains are indeed not directly lifted by the wind friction. The first particles to be
55 mobilized by the wind are the ones whose size is around 115 μm . Bouncing on the surface, these
56 grains (called saltators) start a chain process called saltation. At each impact with the soil other
57 saltators are ejected and the bump can be strong enough to mobilize even the smallest particles
58 (Greeley, 2002). The wind regime needed to start the saltation on Mars is quite uncommon, but,
59 once started the process can be sustained by the typical Martian winds (Almeida et al., 2008;
60 Kok, 2009, 2010).

61 The wind friction and the saltation processes represent the driving lifting mechanisms during
62 the dust storm. However, the lifting power of dust devils appears to be effective in a range of
63 grain size much larger than the one of the wind friction (Neakrase and Greeley, 2010a; 2010b).
64 In addition, the vortices are a continuous source of lifted dust also outside the dust storms season.
65 For these reasons, the dust devils have been proposed as one of the main mechanisms able to
66 sustain the dust haze of the Martian atmosphere (Neubauer, 1966; Thomas and Gierasch, 1985,
67 Klose et al., 2016).

68
69 The pressure gradient force is due to the low-pressure core at the centre of the dust devil. In the
70 simplest and most common case, when the vortex has a single core, the pressure profile can be
71 approximated by a Lorentzian function (Ellehoj et al., 2010):

$$P(t) = \frac{-\Delta P}{1 + \left(\frac{t - t_0}{\frac{1}{2}\Gamma}\right)^2} + B$$

72 where $P(t)$ is the pressure as a function of time, ΔP is the magnitude of the pressure dip at the
73 centre of the vortex, t_0 is the time instant relative to the peak, B is the background pressure value
74 and Γ is the full width at half maximum (FWHM) of the event. The cumulative distribution of
75 the ΔP can be described by a power law function, the magnitude of the drop usually ranges from
76 0.1 to 1.5 mbar (Lorenz and Jackson, 2016).

77
78 The sand and dust grains mobilized by the vortex collide with each other and with the surface,
79 acquiring charge by triboelectricity (Eden and Vonnegut, 1973). When the composition of the
80 colliders is approximatively heterogeneous, the charging process is size-dependent, the smaller
81 grains tending to acquire a charge opposite to the larger ones (Inculet et al., 2006; Duff and
82 Lacks, 2008; Esposito et al., 2016a; Harrison et al., 2016; Neakrase et al., 2016). The smaller
83 grains are lighter and are driven upwards in the dust column by the air flow, while the larger
84 ones stay closer to the ground producing a charge separation. The dust devil can acquire a strong
85 electric field in this way, as firstly reported by Freier (1960), Crozier (1964, 1970). Farrell (2004)
86 has reported for terrestrial dust devils a vertical electric field over 4000 V/m. Taking into account
87 that usually the background absolute value of the terrestrial atmospheric electric field is below
88 100 V/m, the electrical variation due to the passage of a dust devil is a clearly recognizable
89 feature of the event.

90
91 As already mentioned, the role and importance of dust devils in the Martian climate is a highly
92 studied and debated subject. The study of dusty vortices is one of the scientific questions to be
93 pursued by the next Mars space missions, such as the ExoMars 2020 and InSight 2018 (Lorenz,
94 2016). Therefore, the ability to discriminate dust devils in the acquired data becomes of great
95 importance.

96
97 Overall, the main signatures of the passage of a dust devil are (Balme and Greeley, 2006):
98

- 99 - a peak in wind speed,
- 100 - a change in wind direction,
- 101 - a drop in pressure,
- 102 - a peak in the electric field,
- 103 - a peak in concentration of the lifted dust and sand,
- 104 - a raise in atmospheric temperature.

105

106 Depending on the distance to the dust devil and on its magnitude, these features can be more or
107 less evident and some of them may be totally hidden. Clearly, the simultaneous occurrence of
108 all of them strongly indicates the passage of a dusty vortex. The detection of dust devils starts
109 from the search for one of these features. Usually, the variation in the pressure signal is chosen
110 as the main parameter to investigate (Murphy et al., 2016).

111
112 Methods based on the comparison between a short-term and a long-term average are used to
113 detect the isolated drops. This approach is called “phase picker”. In dust devils the long-term
114 average is usually in the order of ten minutes, while the short-term is in the order of ten seconds
115 or less. When the difference between the two values exceeds a chosen threshold the event is
116 counted as a possible dust devil. The threshold depends on the fluctuations around the long-
117 mean value, namely, on the variability and noisiness of the signal. Subsequent check of the other
118 physical parameters allows the elimination of non-significant events. This method is used, with
119 some variants, both on terrestrial (e.g., Jackson and Lorenz, 2015) and on Martian (e.g., Ellehoj
120 et al., 2010) measurements.

121
122 Here we want to propose an alternative technique based on a time-signal adapted operator
123 analysis, instead of the direct time analysis. This technique allows us to deal with very noisy
124 signals and it is less sensitive to the duration and magnitude of the dust devil’s signal, leading
125 to a detection much less sensitive to the choice of arbitrary thresholds. This tool also allows to
126 filter the signal eliminating any component that does not belong to the dust devil.

127
128 The pressure profile of the vortex has a clear shape in the time domain but has no characteristic
129 track in the frequency domain. Therefore, we need a signal transform that takes into account
130 transients and allows the extraction of the signal components that are related to the characteristic
131 behaviour of the dust devils. For this purpose, we decided to adopt a bilinear transformation
132 called tomogram, improving the technique and adapting it to the specific case of the vortices
133 detection.

134
135 The analysed data were acquired during a field campaign performed in Morocco in 2013.
136 The campaign was carried out in the frame of the DREAMS project, the meteorological station
137 on board of the Schiaparelli lander of the ExoMars 2016 space mission (Esposito et al. 2017).
138 We show the results of the application of this new methodology to the data acquired during
139 five days of measurement. We have also analysed the same days with a time-domain
140 technique. Comparing the corresponding results obtained by the two methods, we can test the
141 effectiveness of the tomographic technique.

142 143 2. MATERIAL AND METHODS

144 145 2.1. Field Campaign

146
147 The field campaign took place in 2013 in the Tafilalt region (Morocco) in the north-western
148 Sahara. This area is characterized by an arid environment, it is rich in both sand and dust, and
149 is very active from an aeolian point of view. Measurements have been performed during the
150 dust storm season in a period between July and September at geographical coordinates 4.113°
151 W, 31.161° N, elevation of 797 m a.s.l.

152
153 From the geological point of view, this site is a flat Quaternary lake sediment bed. The sand, silt
154 and clay fractions of the soil have similar composition consisting of detrital shale grains, quartz
155 and carbonates. The position near the centre of the lake made the site rich in hygroscopic and
156 soluble minerals. For this reason, most of the soil grains are aggregated in an extended saline
157 crust.

158 A fully equipped meteorological station (Fig. 1) was deployed consisting of:

- 159
160 - soil temperature (CS thermistor) and moisture (CS616-C) sensors,

- 161 - three 2D sonic anemometers (Gill WindSonic) placed at 0.5, 1.41, 4 m,
162 - one temperature and humidity sensor (Vaisala HMP155) at 4.5 m and one thermometer
163 (Campbell Sci. (CS)) placed at 2.5 m,
164 - pressure sensor (Vaisala Barocap PTB110) at 2 m,
165 - solar irradiance sensor (LI-COR LI-200 Pyranometer) at 4 m,
166 - atmospheric electric field sensor (CS110) faced down at 2 m.

167

168 In addition, to monitor the sand and grain motion were deployed also:

169

- 170 - a size-resolved airborne dust concentration sensor at 1.5 m (Grimm EDM 164-E) that
171 analyses dust in 31 channels in the range 0.265- 34 μm ,
172 - two sand impact sensors (Sensit Inc.) for the detection of saltating sand grains,
173 - three sand catchers (BSNE) at different heights (12, 25 and 40 cm) for daily collection
174 of sand in saltation.

175

176 The station was set to operate 24 hours/day at a sampling rate of 1 Hz. A solar panel system
177 powered the station. Further details on the site and on the field campaign measurements can be
178 found in Esposito et al. (2016a).

179



180

181

Fig. 1: Meteorological station deployed in the Moroccan desert

182

183

2.2. The tomographic technique

184

185 Integral transforms are useful tools for signal analysis in many fields of science, the Fourier
186 transform (Fourier, 1988) and the Wavelet transform (Daubechies, 1990) being among the most
187 popular of these transforms. However, the Fourier transform does not provide information on
188 the transient behaviour of the signal, as time information is spread over the phases of the
189 transform coefficients. Wavelet transform provides some localization but it presents problems
190 in the interpretation of the coefficients and is not an appropriate tool for signals that do not

191 present a multi-resolution behaviour. Localized transforms, such as the Windowed Fourier
 192 transform, allow some localization of the transform coefficients, but require a compromise in
 193 the size of the window due to the Heisenberg uncertainty principle for signals (Donoho and
 194 Stark, 1989). Shorter window sizes, allow a good localization in time but reduce the capacity of
 195 detection of low frequency components in the signal, on the other hand, longer window sizes
 196 reduce the capacity of time localization of the transform.

197

198 Bilinear transforms are frequently used to provide information in the time-frequency domain.
 199 Among these transforms, the Wigner-Ville quasi-distribution (Wigner, 1932) is the most
 200 commonly used. The Wigner-Ville quasi-distribution has the problem that spurious or even
 201 negative terms also appear in areas where there is no signal at all. The Wigner-Ville quasi-
 202 distribution can be seen as a windowed version of the Wigner-Ville distribution and presents
 203 the same problems of compromise in the size of the window as the Windowed Fourier
 204 Transform. The Wigner-Ville quasi-distribution does not guarantee the absence of spurious
 205 terms and may present a meaningless spread in the physically correct time-frequency regions.

206

207 These problems in the bilinear transforms arise from the fact that time and frequency are two
 208 noncommutative operators and therefore a joint probability distribution cannot be defined, even
 209 in the case of positive quasi probabilities, such as the Husimi-Kano function (Husimi, 1940;
 210 Kano, 1965).

211

212 Tomograms (Man'ko and Mendes, 1999) are strictly positive bilinear transforms. They are a
 213 generalization of the Radon transform to arbitrary pairs of non-commutative operators, the
 214 Radon-Wigner transform being a particular case of a tomogram. These transforms are strictly
 215 positive probability densities that provide a full characterization of the signal. A complete
 216 characterization of the tomogram transforms may be found in Man'ko et al. (2001). The
 217 transforms are obtained from the projections on the eigenstates of self-adjoint operators B
 218 obtained as a linear combination of a pair of commuting or non-commuting operators O_1 and
 219 O_2 .

220

221

$$B(\mu, \nu) = \mu O_1 + \nu O_2$$

222

223 Following this method, tomograms have been built for several pairs of operators. Of special
 224 interest is the time-frequency operator:

225

$$B_{tf}(\mu, \nu) = \mu t + \nu \omega = \mu t + \nu \left(-i \frac{\partial}{\partial t}\right)$$

226

227 Taking $\mu = \cos(\theta)$ and $\nu = \sin(\theta)$ one obtains an operator that depends on a single value $\theta \in$
 228 $(0, \pi/2)$ interpolating between the time and frequency operators:

229

230

$$B_{tf}(\theta) = \cos(\theta) t + \sin(\theta) \left(-i \frac{\partial}{\partial t}\right)$$

231

232 When $\theta=0$ we are in the time domain and when $\theta= \pi/2$ we are in the frequency domain.

233

234 The construction of the time-frequency tomogram reduces to the calculation of the generalized
 235 eigenvectors of the operator B_{tf} . For example, the projection $M_f(\theta, X)$ for a finite time signal
 236 $f(t)$ defined in an interval t_0 to t_0+T is:

237

238

$$M_f(\theta, X) = \left| \int_{t_0}^{t_0+T} f^*(t) \psi_{\theta, X}(t) dt \right|^2 = |\langle f, \psi \rangle|^2$$

239

240

where $\psi_{\theta, X}(t)$ are the eigenfunctions of operator B_{tf} , namely

241

$$\psi_{\theta,x}(t) = \frac{1}{\sqrt{T}} \exp\left(\frac{i \cos \theta}{2 \sin \theta} t^2 + \frac{iX}{\sin \theta} t\right)$$

242

243

244

245

246

247

248

249

250

251

252

253

254

255

256

257

258

259

260

261

262

263

264

265

266

267

268

269

270

271

272

273

$$B(\mu, \nu) = \mu t + \nu O$$

274

275

276

277

278

279

280

281

282

283

284

285

286

287

$$U = \begin{pmatrix} x_1(1\Delta t) & x_1(2\Delta t) & \cdots & x_1(N\Delta t) \\ \vdots & \ddots & & \vdots \\ x_k(1\Delta t) & x_k(2\Delta t) & \cdots & x_k(N\Delta t) \end{pmatrix}$$

288

289

290

291

292

Time-frequency tomograms have already been used to remove noise and separate the signal components in many scientific fields. For example, in (Briolle et al., 2012) time-frequency tomograms were used for plasma reflectometry and in (Aguirre et al., 2013) neuronal signatures (i.e, characteristic time patterns in firing neurons that conform a specific message to other neurons) are detected by means of tomography.

The concept of signal component is not uniquely defined and the notion of a component depends not only on the observed signal but also on the specific features that we are interested on. A signal component might, for example, be a component with some specific signature in the time or in the frequency domain. However, signal components are not always easy to define as time or frequency signatures, and sometimes there is not a simple analytical description of the component that we are looking for. Even if a clear description is available, the component can be still hidden by noise. This makes the separation in the time domain a difficult issue. Moreover, in the frequency domain the component might not have a characteristic signature and be hidden by other components.

The dust devils pressure drop has a clear time behaviour (as mentioned in introduction). This trend, due to the atmospheric pressure variation, could be totally or partially hidden by noise. Moreover, in the frequency domain, dust devils pressure does not possess a characteristic behaviour. This fact suggests that a different kind of tomograms should be used. In this new tomogram one of the operators should be adapted to the characteristics of the component we want to separate.

A new type of signal-adapted tomogram has recently been proposed by (Aguirre and Vilela Mendes, 2014) with the detection of dust devils in mind (Gimenez-Bravo et al., 2013). The signal-adapted tomogram is a linear combination of a standard operator, such as time or frequency with an operator O that is specially tuned to the features of the component that one wants to extract:

As in the time-frequency tomogram a particular set of (μ, ν) pairs can be selected by a single parameter θ , with $\mu = \cos \theta$, $\nu = \sin \theta$. It is possible to separate the signal components we are interested in from the noise components by looking for particular values of θ where noise or undesired components cancel or becomes small, as high concentration of energy in some coefficients of the transform means that the signal contains the component we are looking for. This has the additional advantage that we can retain information about the temporal structure of the signal. The construction of signal-adapted operators follows the same technique as used in the bi-orthogonal decomposition of signals (Aubry et al., 1991, Dente et al., 1996).

Consider a set of k N -dimensional time sequences $\{\vec{x}_1, \vec{x}_2, \dots, \vec{x}_k\}$ that are typical representations of the component one wants to detect. This set of time sequences can be represented by means of a $k \times N$ matrix U , with usually $k < N$:

We now construct the square matrix:

$$A = U^T U \in \mathcal{M}_{N \times N}$$

293 The diagonalization of A provides k non-zero eigenvalues ($\alpha_1, \alpha_2, \dots, \alpha_k$) and the corresponding
 294 k N-dimensional eigenvectors ($\Phi_1, \Phi_2, \dots, \Phi_k$).

295

296 Now a linear operator S can be constructed from the previous set of eigenvectors in the following
 297 way:

298

$$299 \quad S = \sum_{i=1}^k \alpha_i \Phi_i \Phi_i^T \in \mathcal{M}_{N \times N}$$

300

301 To construct the time-data tomogram we build the time operator for discrete time in the
 302 following way:

303

$$304 \quad t = \begin{pmatrix} 1\Delta t & & & \\ & 2\Delta t & & \\ & & \ddots & \\ & & & N\Delta t \end{pmatrix} \in \mathcal{M}_{N \times N}$$

305

306 and to generate the tomogram we consider a linear operator B(μ, ν) of the form:

307

$$308 \quad B(\mu, \nu) = \mu t + \nu S = \mu \begin{pmatrix} 1\Delta t & & & \\ & 2\Delta t & & \\ & & \ddots & \\ & & & N\Delta t \end{pmatrix} + \nu \sum_{i=1}^k \alpha_i \Phi_i \Phi_i^T \in \mathcal{M}_{N \times N}$$

309

310 As usual, parameters μ and ν are considered in the form $\mu = \cos \theta$, $\nu = \sin \theta$.

311

312 Now proceeding in a way like the time-frequency operator, we obtain the N eigenvectors
 313 $\{\bar{\Psi}_\theta^1, \bar{\Psi}_\theta^2, \dots, \bar{\Psi}_\theta^N\}$ of operator B(θ). Projections of the signal \bar{X} on these eigenvectors are obtained
 314 by

315

$$316 \quad c_\theta^i = \langle \bar{X}, \bar{\Psi}_\theta^i \rangle \text{ for } i = 1, 2, \dots, N$$

317

318 These projections construct a tomogram adapted to the operator pair t, S.

319

320 Once the tomogram is constructed, the signal can be denoised or decomposed just by
 321 considering the set of values that contain a given amount of the total energy of the signal or by
 322 considering only the coefficients with an absolute value over a given threshold $c_\theta^i \geq \epsilon$ with ϵ
 323 being a fixed threshold or a function that depends on the whole set of coefficients $\{c_\theta^1, c_\theta^2, \dots, c_\theta^N\}$.

324 In this work ϵ is taken as a fixed value multiplied by the spectrum average $\frac{1}{N} \sum_{j=1}^N |c_\theta^j|$, this is

325

$$326 \quad \epsilon = k \frac{1}{N} \sum_{j=1}^N |c_\theta^j|$$

327

328 If we consider only the indexes $i = i_1, i_2, \dots, i_h$ for which $c_\theta^i \geq \epsilon$ we obtain a subset of h
 329 coefficients $C = \{c_\theta^{i_1}, c_\theta^{i_2}, \dots, c_\theta^{i_h}\}$. Signal \bar{x}^f is now reconstructed by considering only the
 330 vectors $\{\bar{\Psi}_\theta^{i_1}, \bar{\Psi}_\theta^{i_2}, \dots, \bar{\Psi}_\theta^{i_h}\}$ of the tomogram that are in subset C, this is:

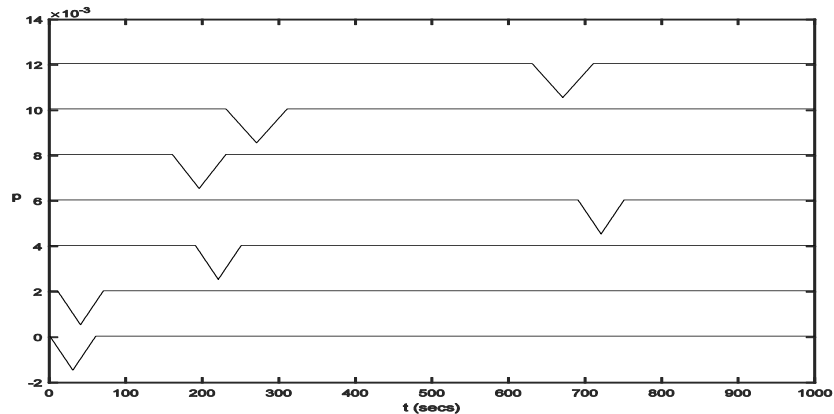
331

$$332 \quad \bar{x}^f = \sum_{j=1}^h c_\theta^{i_j} \bar{\Psi}_\theta^{i_j}$$

333
334
335

2.3. Event detection

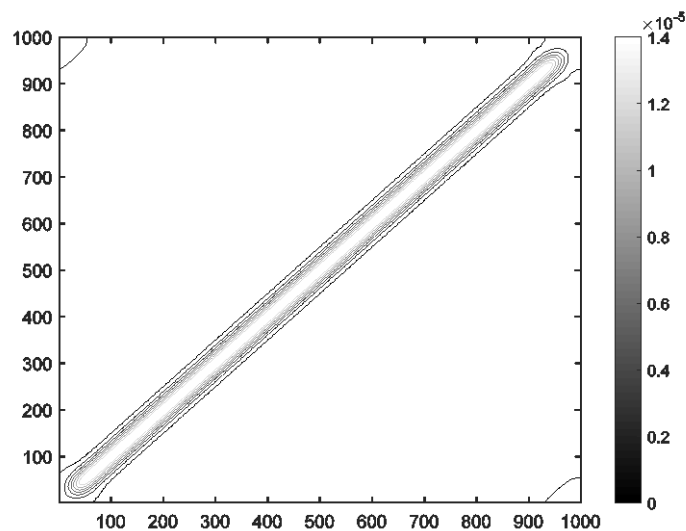
336 As dust devils produce a drop in the pressure value we have built a 277x1000 matrix U that
337 contains a set of 277 typical signals of 1000 second duration, containing a drop of 15% from the
338 baseline with durations ranging from 20 to 60 seconds and normalized to zero mean. With this
339 method, the amount of drop is not significant so we have selected a drop that works well in
340 many environments, for example this set of signals could be used in atmospheres with a lower
341 pressure level or dust-devil like phenomena produce a higher drop in the pressure signal, as
342 happens in Mars atmosphere. In Fig. 2 a set of several of this type of signals shifted in value for
343 a better view is depicted.



344
345
346

Fig. 2: Sample set of normalized to zero mean typical signals.. Time is measured in seconds and p represents normalized pressure. Some signals are shifted in value for a better view.

347 From the Matrix U we build Matrix A and finally we build the *signal-adapted* operator S as
348 described in the previous section. Fig. 3 is a plot of the signal-adapted operator S; each point in
349 the plot represents a value in matrix S, showing that operator is symmetric and definite positive.



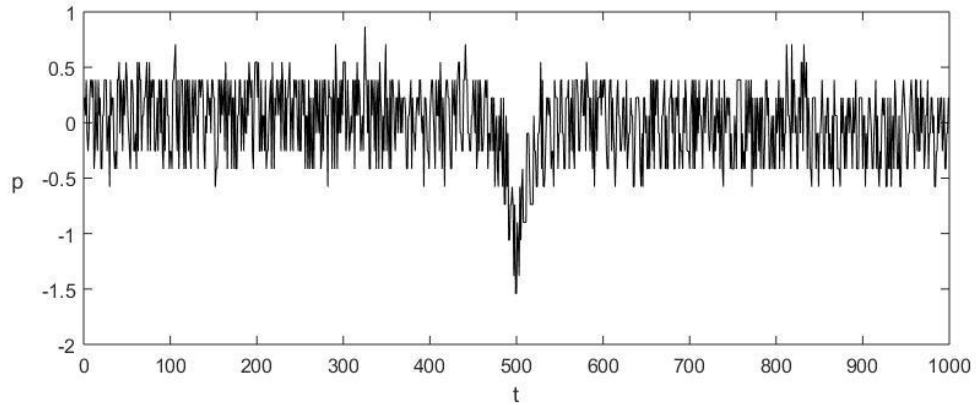
350
351
352

Fig. 3: The signal-adapted operator Matrix S.

353
354
355
356

Finally, we build the tomogram with the linear combination $B(\theta) = \cos(\theta)t + \sin(\theta)S$ for the values $\theta = \frac{\pi l}{40}$ $l = 1, 2 \dots 20$.

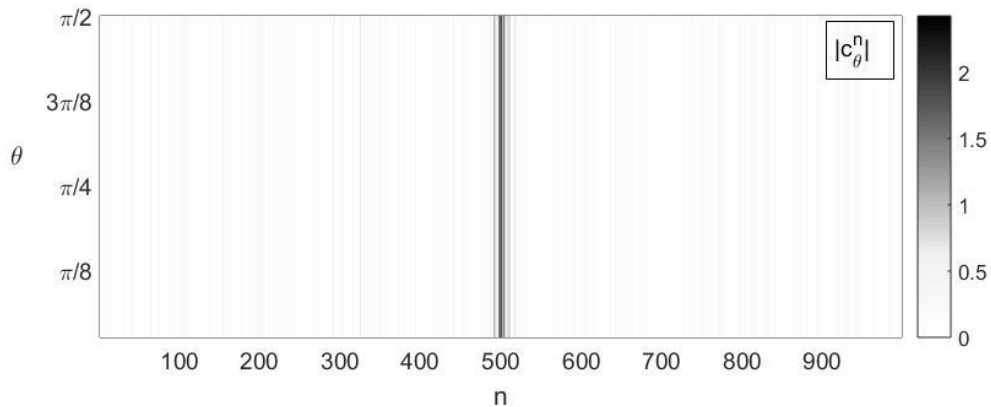
357 We break up our signal in 1000-second samples with a 200-second margin from the previous
 358 sample to avoid losing events close to the border. To avoid high-energy coefficients in the
 359 transform we normalize the signals to zero mean. In Fig. 4 a 1000-second sample with a possible
 360 dust devil event is depicted (observed at '2013-08-10 16:44:39').
 361



362

363 *Fig. 4: Pressure data containing a possible dust devil event observed at '2013-08-10 16.7441667, 16:44:39'. Signal*
 364 *is normalized to zero mean to avoid high energy coefficients.*

365 In Fig. 5 a plot of the $B(\theta)$ -tomogram applied to the previous sample is depicted. For all values
 366 of θ there exists a clear peak close to coefficient c_{θ}^{500} .
 367

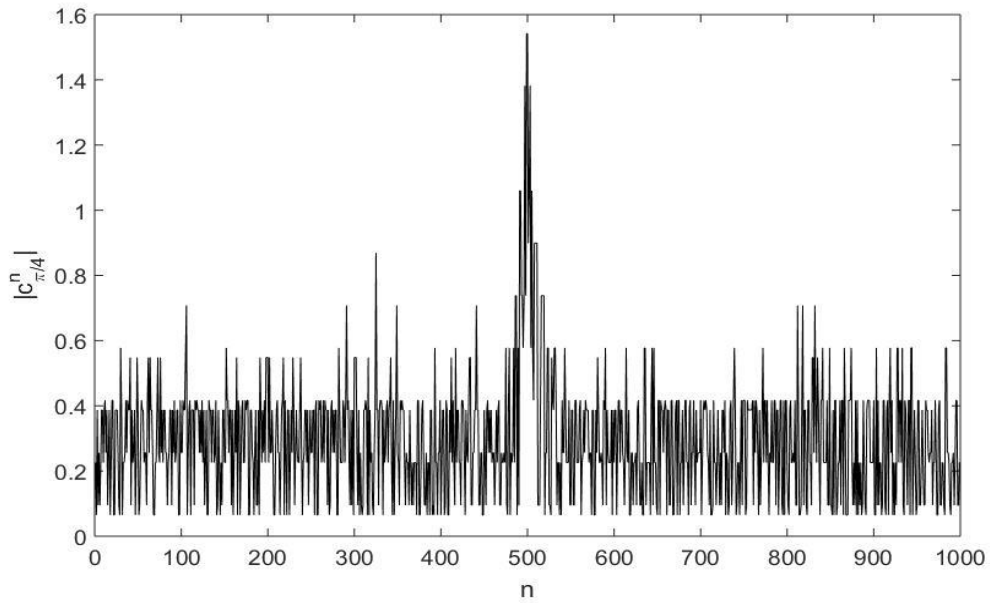


368

369 *Fig. 5: Plot of the tomogram for pressure data. A clear peak is visible at coefficient c_{θ}^{500} for most values of θ .*

370 In Fig. 6 the projection of the data for $\theta = \frac{\pi}{4}$ is depicted showing that, effectively a clear peak
 371 exists close to the coefficient $c_{\frac{\pi}{4}}^{500}$. In order to avoid border effects, the first and last coefficient
 372 of the projection are discarded, as these coefficients tend to concentrate the energy of the signal
 373 that does not correspond to dust devil events. To detect relevant events any standard filtering
 374 technique can be applied, for example, you can consider coefficients that are over a given fixed
 375 threshold or coefficients that are clearly over the average value of the transformed signal. Higher
 376 values of the coefficients correspond to clearer dust devil events.
 377

378



379

380

Fig. 6: Projection of the pressure data tomogram for $\theta = \frac{\pi}{4}$.

381

382

383

384

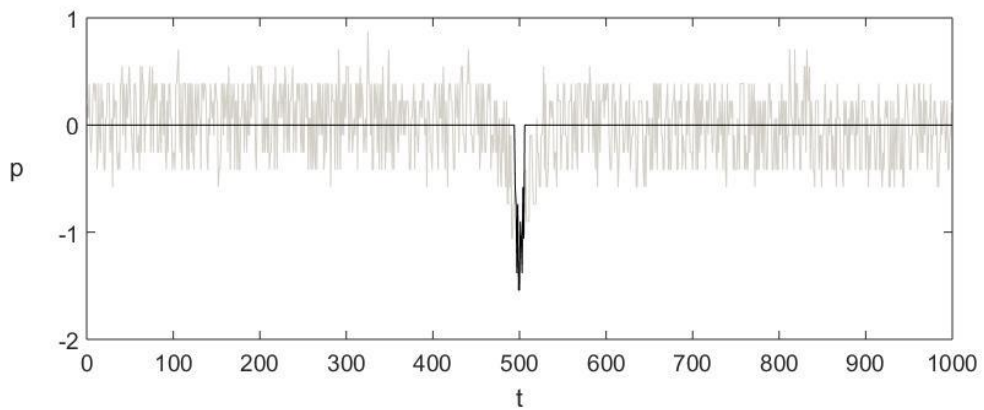
385

386

387

388

We can now filter the signal just keeping a small set of values close to the most significant value and reconstructing the dust devil component. In Fig. 7 a reconstruction from coefficients from $c_{\frac{\pi}{4}}^{495}$ to $c_{\frac{\pi}{4}}^{505}$ is depicted. It can be observed that any component of the signal that does not behave as a dust devil is removed. To obtain the duration of the dust devil just consider the values that are different from zero, and to obtain the pressure drop just de-normalize the filtered signal.



389

390

391

Fig. 7: Original (gray) and reconstructed (black) signal from coefficients from $c_{\frac{\pi}{4}}^{495}$ to $c_{\frac{\pi}{4}}^{505}$ of event T38 detected at '2013-08-10 16:7441667, 16:44:39'.

392

393

394

395

396

397

398

As explained in Section 2.2, to identify the dust devil components of the signal we make use of the spectrum average, this is $\frac{1}{N} \sum_{j=1}^N |c_{\theta}^j|$, where c_{θ}^j are coefficients of the tomographic transform of the signal. The clearer the dust devil event is, the bigger is the corresponding coefficient or set of coefficients in the tomographic transform, so we classify the dust devil event depending of the relative size with the spectrum average. As can be seen in Fig. 5, the event can be clearly detected for any value of θ , and therefore we have opted for the simplest solution of taken a fixed value of $\theta = \frac{\pi}{4}$.

399
400
401
402
403

The detected events have been divided into classes from the least probable to the most probable depending on the relative magnitude of the transform coefficient from the spectrum average. We labelled the events with an ID that starts with T. The classification used is in Table 1.

| Tomography technique | |
|----------------------|--|
| Classes | Main Characteristics |
| E | Transform coefficient $> 6 \cdot$ spectrum average |
| D | Transform coefficient $> 6,5 \cdot$ spectrum average |
| C | Transform coefficient $> 7 \cdot$ spectrum average |
| B | Transform coefficient $> 7,5 \cdot$ spectrum average |
| A | Transform coefficient $> 8 \cdot$ spectrum average |

404

Table 1 Classes and main characteristics regarding the division of the events identified by the Tomography technique.

405
406
407

2.4. Time domain research technique

408
409
410
411
412
413
414
415
416
417
418
419
420

We want to compare the results obtained by the tomography method with those obtained by the direct analysis of the time domain signal.

In order to detect the passage of a dust devil in the data we have compared a long term with a short-term mean, to determinate the fast variations in the signal. This kind of analysis, called “phase picker”, is the most common for the dust devil detection and is usually performed on the atmospheric pressure time series (Lorenz and Jackson, 2016). Indeed, as we have seen (eq. 1), the pressure variation is a distinctive characteristic of the dust devil encounters. The passage of the vortex lasts only a few seconds in the data, so both the long-term time interval and the short one have to be as short as possible. Our choice of the long-term mean, 12 minutes, is similar to the one commonly used in literature (e.g. Jackson and Lorenz 2015). The standard deviation of the pressure measurements around this long term is on average of 0.3 mbar. This noise level is too high to allow a clear detection of the medium magnitude signals and it could totally cover the weaker encounters.

421
422
423
424
425
426

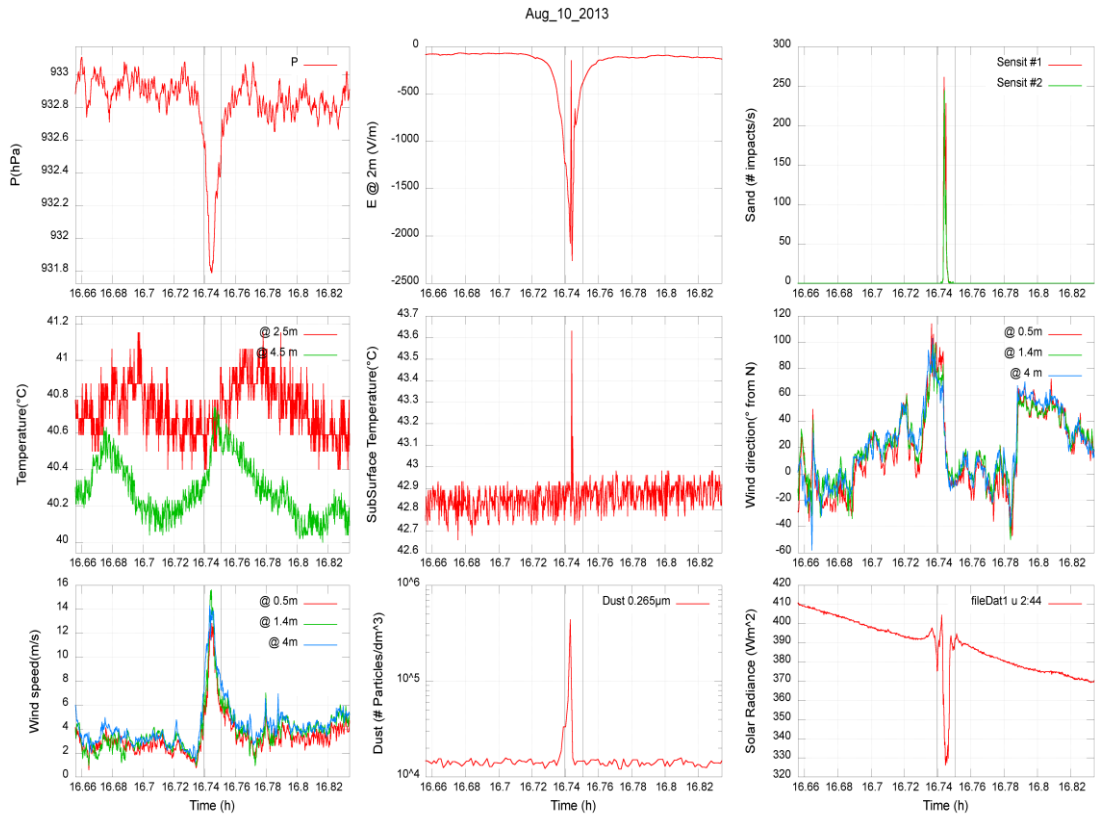
In order to use the standard phase picker method on the pressure time series we need to filter the noise. For this purpose, we have used a running average on a time window of 11 seconds. The extension of the window would lead to a further cut of the noise but also to a reduction of the drop magnitude, until the complete elimination of the dust devils signals. After the application of the filter the standard deviation around the long-term mean is on average of 0.1 mbar; we can use then our measurements taken at 1 Hz rate as the short term values.

427
428
429
430
431
432
433
434
435
436
437
438
439

We have developed software that analyses the filtered data, dividing the whole day in time intervals of 12 minutes. For each one it evaluates the median value of the atmospheric pressure. When the instantaneous pressure value and the median one differ for more than a given limit (ΔP_{lim}), the event is selected. In the following, we will refer to these detections as class T events. However, the detection of an isolated pressure drop is not enough to confirm the events as dust devil, indeed we need the simultaneous occurrence of one or more other meteorological signatures described in section 1. For this reason, the software analyses the variations of wind direction and electric field during the selected events. If both these variations overcome the chosen thresholds, ΔW_{lim} and ΔE_{lim} , the event is identified as a dust devil. We have used the following values for the limits: $\Delta P_{lim}=0.18$ mbar, $\Delta W_{lim}=30^\circ$, $\Delta E_{lim}= 50$ eV. Indeed, these values give a good compromise between the possibility of detecting even the small dust devils and the ability to cut off the main part of the non-significant events. For further explanation on the method, see Franzese et al. (2017).

440
441

Fig. 8 shows how one of the detected events (the same event of Fig. 7) appears in the whole set of measured parameters.



442
443

Fig. 8: A dust devil at '2013-08-10 16.7441667, 16:44:39' identified by the meteorological instruments.

444
445
446
447
448
449

Here we are not interested in testing the reliability of the phase picker technique, but we are looking for possible dust devils not seen by the tomographic technique. Hence we decided to classify the events after a crosscheck of every measured parameter, in order to verify if they are or not true dust devils. We have used the classes shown in Table 2, labelling the events with an ID that starts with P.

| Time domain research technique | |
|--------------------------------|---|
| Classes | Main Characteristics |
| D | The event is a false positive, where the dust devils features are certainly not recognizable. |
| C | The pressure drop is barely observable and there are weak variations in electric field, wind speed and direction. The signal usually shows also features hardly compatible with a dust devil, i.e., a peculiar shape or anomalous time duration. The event probably is not a dust devil |
| B | The magnitude of the pressure drop is comparable with the noise level so could be partially hidden. However, the event shows a clear peak for each of the other main parameters. The event is probably a dust devil |
| A | The event shows a clear peak for each of the main parameters, it is clearly recognizable as a dust devil |

450
451

Table 2 Classes and main characteristics regarding the division of the events identified by the time domain research technique performed on three parameters (pressure, wind direction and electric field).

452
 453
 454
 455
 456
 457
 458
 459
 460
 461
 462
 463
 464
 465
 466
 467
 468
 469
 470
 471

3. RESULTS AND DISCUSSION

In this section, we show the results obtained through the application of two research techniques. Our purpose is to evaluate the reliability and effectiveness of the tomography. For this reason, we have initially crosschecked all the events identified by the tomography, through the analysis of the entire set of meteorological parameters, in order to confirm if the dust devil's signatures are recognizable or not. Then we have compared the results of the tomography with those obtained by the direct time domain research.

The tomography technique has identified 47 dust devils candidates: 12 class E, 21 class D, 3 class C, 7 class B and 4 class A events. The crosscheck of these events confirms that all the class A events are recognizable as dust devils, while all the class E ones are not. Regarding the class B events, just one seems not to be a dust devil, while, there are two other "not dust devil" events in the class C. Three of the class D events are recognizable as dust devils, 4 seem to be not a dusty convective vortex, while the remaining ones appear to be wind gusts or related to dust storms.

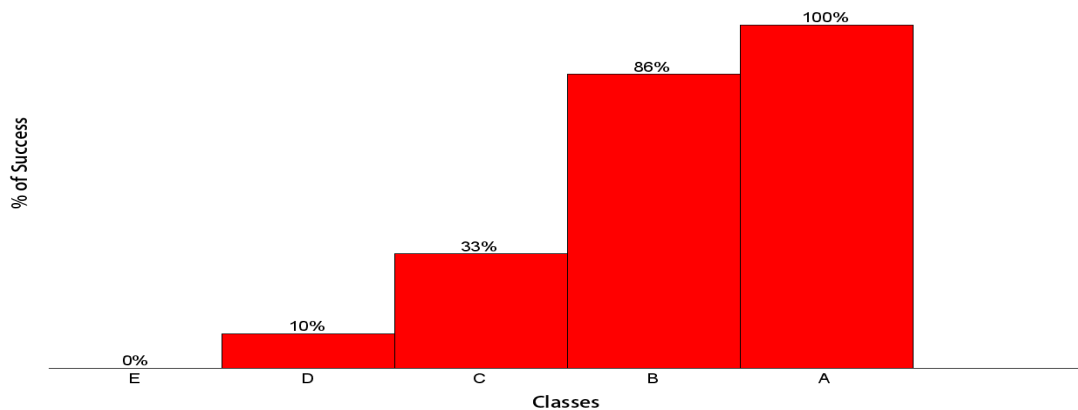
The complete list of the detected events and the results of the manual check are given in Table 3.

| ID | Date | ti(h) | Tomograms Class | Full parameters Crosscheck |
|-----|------------|------------|-----------------|----------------------------|
| T1 | 17_07_2013 | 4.7944445 | E | No |
| T2 | 17_07_2013 | 4.8316667 | E | No |
| T3 | 17_07_2013 | 4.8650000 | E | No |
| T4 | 17_07_2013 | 5.0838889 | E | No |
| T5 | 17_07_2013 | 5.1352778 | D | No |
| T6 | 17_07_2013 | 5.4038889 | D | No |
| T7 | 17_07_2013 | 5.4352778 | D | No |
| T8 | 17_07_2013 | 7.0977778 | E | No |
| T9 | 17_07_2013 | 9.6669445 | E | Not dusty Vortex |
| T10 | 17_07_2013 | 14.0333333 | E | No |
| T11 | 17_07_2013 | 15.5966666 | D | Yes |
| T12 | 17_07_2013 | 15.8788889 | D | Not dusty Vortex |
| T13 | 17_07_2013 | 16.0333333 | D | No |
| T14 | 17_07_2013 | 18.9736111 | A | Yes |
| T15 | 17_07_2013 | 19.5730556 | D | No |
| T16 | 17_07_2013 | 20.0319444 | D | No |
| T17 | 17_07_2013 | 20.5786111 | B | No |
| T18 | 17_07_2013 | 20.6494444 | B | Yes |
| T19 | 17_07_2013 | 21.5641667 | A | Yes |
| T20 | 21_07_2013 | 8.4327778 | D | No |
| T21 | 21_07_2013 | 12.8000000 | A | Yes |
| T22 | 21_07_2013 | 13.3691667 | B | Yes |
| T23 | 21_07_2013 | 14.9480556 | D | No |
| T24 | 21_07_2013 | 15.7708333 | D | No |
| T25 | 21_07_2013 | 18.6238889 | D | No |
| T26 | 24_07_2013 | 8.7080555 | D | No |
| T27 | 24_07_2013 | 9.0041667 | D | Not dusty Vortex |

| | | | | |
|-----|------------|------------|---|------------------|
| T28 | 24_07_2013 | 9.6888889 | B | Yes |
| T29 | 24_07_2013 | 10.9250000 | B | Yes |
| T30 | 24_07_2013 | 11.0016667 | D | Possible |
| T31 | 24_07_2013 | 11.5891666 | D | Yes |
| T32 | 24_07_2013 | 16.8805556 | B | Yes |
| T33 | 10_08_2013 | 0.0497222 | E | No |
| T34 | 10_08_2013 | 4.8011111 | E | No |
| T35 | 10_08_2013 | 11.9986111 | D | No |
| T36 | 10_08_2013 | 12.2894444 | D | No |
| T37 | 10_08_2013 | 13.9894444 | D | Not dusty Vortex |
| T38 | 10_08_2013 | 16.7441667 | A | Yes |
| T39 | 10_08_2013 | 17.9986111 | D | No |
| T40 | 11_08_2013 | 1.9922222 | E | No |
| T41 | 11_08_2013 | 3.9872222 | E | No |
| T42 | 11_08_2013 | 5.9919444 | E | No |
| T43 | 11_08_2013 | 9.9916667 | D | Not dusty Vortex |
| T44 | 11_08_2013 | 11.4319444 | B | Yes |
| T45 | 11_08_2013 | 13.0125000 | C | Yes |
| T46 | 11_08_2013 | 13.9905556 | C | No |
| T47 | 11_08_2013 | 19.9902778 | C | No |

472 **Table 3** List of the events identified with the tomography technique. The date, the initial instant, the tomogram class
473 and the result of the manual crosscheck are reported. The results of the crosscheck are simply given in term of yes
474 and no, except one case for which the meteorological data is not conclusive and the event is catalogued as possible.
475 We also indicate the events recognizable as convective not dust loaded vortices.

476
477 The signal-adapted tomogram used in this work was constructed for the pressure time series
478 only. Therefore, in theory, this method has no possibility of distinguish between the dusty and
479 the not dusty vortices. However, any of the detected “not dust loaded vortices” belong to the
480 most probable classes A and B, they all fall in the lower classes D and E.
481 Fig. 9 shows the number of true dust devils in every class normalized by the number of events
482 in the class. It is clear how the percentage of true dust devils in every class rapidly grows towards
483 the A class and it is highly probable that the events belonging to the higher class A and B
484 are true dust devils. This proves the affability of the tomography technique and the reliability of the
485 chosen classification.



486
487 **Fig. 9:** The percentage of true dust devils, recognized by the full parameters crosscheck, for every class of the
488 tomographic analysis.

489 As said, the small values of the thresholds that we are using have the advantage of detecting
 490 even the smaller dust devils. On the other hand, this increases the number of false detections.
 491 Out of the 361 dust devils candidates, 328 are non-significant events (class D). Of the remaining
 492 23 detections, 6 are class C, 2 are class B and 15 are class A events. We report in Table 4 only
 493 the possible dust devils (class A, B and C).
 494

| ID | Date | ti (h) | Δt (s) | S (counts/s) | ΔW_{dir} (°) | ΔP (mbar) | Classes |
|-----|------------|---------|----------------|-----------------|-------------------------|----------------------|---------|
| P1 | 17_07_2013 | 12.115 | 6.1 | 0.2 | 45 | 0.4 | A |
| P2 | 17_07_2013 | 13.0614 | 9.0 | 0.0 | 31 | 0.3 | B |
| P3 | 17_07_2013 | 13.7617 | 18.7 | 0.0 | 175 | 0.3 | A |
| P4 | 17_07_2013 | 15.595 | 23.0 | 1.4 | 31 | 0.5 | A |
| P5 | 17_07_2013 | 17.1817 | 4.0 | 2.1 | 34 | 0.3 | C |
| P6 | 17_07_2013 | 17.8178 | 4.0 | 3.1 | 41 | 0.3 | C |
| P7 | 17_07_2013 | 18.9661 | 45.0 | 3.6 | 94 | 0.8 | A |
| P8 | 17_07_2013 | 20.5736 | 37.1 | 0.9 | 52 | 0.7 | C |
| P9 | 17_07_2013 | 20.6439 | 36.0 | 12.8 | 42 | 0.7 | A |
| P10 | 17_07_2013 | 21.3003 | 38.9 | 152.5 | 60 | 0.6 | C |
| P11 | 17_07_2013 | 21.5617 | 34.9 | 35.9 | 164 | 1.3 | A |
| P12 | 17_07_2013 | 22.0197 | 12.2 | 5.3 | 36 | 0.3 | C |
| P13 | 17_07_2013 | 22.0675 | 29.9 | 8.0 | 51 | 0.5 | B |
| P14 | 21_07_2013 | 12.7928 | 41.8 | 0.0 | 179 | 0.8 | A |
| P15 | 21_07_2013 | 13.3683 | 13.0 | 5.9 | 80 | 0.5 | A |
| P16 | 21_07_2013 | 18.5372 | 13.0 | 0.4 | 37 | 0.4 | C |
| P17 | 24_07_2013 | 9.68722 | 12.0 | 0.0 | 53 | 0.4 | A |
| P18 | 24_07_2013 | 10.9225 | 24.8 | 0.1 | 92 | 0.7 | A |
| P19 | 24_07_2013 | 11.5881 | 20.9 | 0.0 | 94 | 0.5 | A |
| P20 | 24_07_2013 | 16.8775 | 51.1 | 0.0 | 124 | 0.9 | A |
| P21 | 10_08_2013 | 16.7394 | 41.0 | 24.4 | 116 | 1.0 | A |
| P22 | 11_08_2013 | 11.4311 | 13.0 | 2.9 | 120 | 0.6 | A |
| P23 | 11_08_2013 | 13.0119 | 40.3 | 0.0 | 174 | 0.5 | A |

495 **Table 4** List of the events identified by the time domain research technique. For each events we report the date, the
 496 initial instant (t_i), the time duration (Δt), the mean values inside the event of Sensit counts, the maximum wind speed
 497 direction change (ΔW_{dir}), the pressure drop (ΔP) magnitude and the class.

498
 499 We focused on the best candidates detected by the time domain research (class A and B),
 500 comparing the results with the ones obtained by tomography. As it can be noted in Table 5, the
 501 events detected are in good agreement for all the data. There are only 4 events not detected by
 502 tomography: two class B and two class A, and they all happened during July, 17th. Overall, there
 503 is a match of 12 events over 16. Moreover, there is an event detected only by tomography during
 504 July 24th, recognized by the full parameters crosscheck as a possible dust devil.
 505

506 The first step of the time domain analysis performed only on the pressure parameter has
 507 identified a total of 6611 class T events. Such large number of detections shows that a simple
 508 pressure phase picker analysis is not sufficient to strictly constrain the identification of dust
 509 devils, especially when the noise level is relevant. In order to reduce the number of detected
 510 non-significant events and to identify the true possible dust devil, we have selected the events
 511 that show a synchronous variation of pressure, wind direction and electric field, analysing using
 512 a set of three parameters.

513 On the other hand, the tomography is specifically calibrated to search for the dust devil signature
514 by analysing one single parameter. The tomogram has reached a good efficiency in the detection,
515 providing a clear classification of the events, allowing to individuate the best candidates. In
516 addition, the tomographic analysis can be performed directly on the raw data, despite the
517 presence of high noise level. As described in section 3.3, in order to perform the “phase picker”
518 technique on the pressure data, we had to use a running average filter. Instead, no filtering is
519 needed to perform the tomography, because, as discussed in section 3.2, it is able to eliminate
520 the part of signal that does not belong to the dust devil by analysing the coefficient c_{θ}^i .
521

| Time domain research | | | | | Tomography research | | |
|----------------------|------------|---------|-------|-------|---------------------|---------|-------|
| ID | Date | ti (h) | Class | Match | ID | ti (h) | Class |
| P2 | 17_07_2013 | 13.0614 | B | No | | | |
| P13 | 17_07_2013 | 22.0675 | B | No | | | |
| P1 | 17_07_2013 | 12.115 | A | No | | | |
| P3 | 17_07_2013 | 13.7617 | A | No | | | |
| P4 | 17_07_2013 | 15.595 | A | Yes | T11 | 15.5966 | D |
| P7 | 17_07_2013 | 18.9661 | A | Yes | T14 | 18.9736 | A |
| P9 | 17_07_2013 | 20.6439 | A | Yes | T18 | 20.6494 | B |
| P11 | 17_07_2013 | 21.5617 | A | Yes | T19 | 21.5641 | A |
| P15 | 21_07_2013 | 13.3683 | A | Yes | T22 | 13.3691 | B |
| P17 | 24_07_2013 | 9.68722 | A | Yes | T28 | 9.6888 | B |
| P18 | 24_07_2013 | 10.9225 | A | Yes | T29 | 10.9250 | B |
| P19 | 24_07_2013 | 11.5881 | A | Yes | T31 | 11.5891 | D |
| P20 | 24_07_2013 | 16.8775 | A | Yes | T32 | 16.8805 | B |
| P22 | 11_08_2013 | 11.4311 | A | Yes | T44 | 11.4319 | B |
| P23 | 11_08_2013 | 13.0119 | A | Yes | T45 | 13.0125 | C |
| P14 | 21_07_2013 | 12.7928 | A | Yes | T21 | 12.8000 | A |
| P21 | 10_08_2013 | 16.7394 | A | Yes | T38 | 16.7441 | A |
| | 24_07_2013 | | | No | T30 | 11.0016 | D |

522 *Table 5 The match between the events identified by time domain research technique and by the tomography technique.*

523
524
525

4. CONCLUSIONS

526 We have monitored five days of dust devil activity in the Moroccan Sahara tomogram
527 convective vortex pressure core drop detection. This method combines a time operator with a
528 data adapted operator, built from a set of type signals that represent the behaviour of a dust devil
529 pressure signal. The method is automatic and does not require fine-tuning of its parameters.

530
531 The algorithm has identified a total of 47 events, classifying them in 5 classes (E,D,C,B and A)
532 from the least probable to the most probable as dust devils. We have crosschecked the events
533 by comparison with the behaviour of the other meteorological parameters, confirming that all
534 the class A events are actually dust devils, while all the class E are not significant detections.
535 The tomography has demonstrated an excellent ability to distinguish between the true dust devils
536 and the false positive events, even analyzing only the pressure parameter.

537
538 We have tested the efficiency of our method by comparing it with a standard time domain
539 research technique. For this purpose, we have performed a phase picker detection on the pressure
540 measurements, using an eleven second running average to cut the signal noise. In order to
541 eliminate the false positive events, the phase picker algorithm also analyses the wind direction
542 and electric field, looking for the synchronous occurrence of dust devils features in the three

543 parameters. The tomography has given good results compared to the phase picker technique
544 missing only two high probable dust devils and two probable ones, while it has detected a
545 possible dust devil unseen by the other method. In addition, due to its innate ability to filter the
546 background signal components, the tomography does not require the preliminary processing of
547 the pressure data.

548

549 The study of dust devils is a topic of great interest in Martian science: these vortices are common
550 and widespread along the planet surface, and they give substantial contribution to the global
551 dust emission, affecting the radioactive budget and the global climate.

552

553 However, it is not uncommon that the monitoring of the dust devil's activity by the landed
554 instrument is affected by possible complications. The Viking Meteorology Instrument System
555 on board of the Viking Lander 1, as well as Meteorology Package on board of the Pathfinder
556 lander and the Rover Environment Monitoring Station on board of the Curiosity rover have
557 expired anomalies with the wind speed and direction detectors, making the wind data totally
558 unavailable in some cases. The lack of these key parameters represents a serious issue for the
559 unambiguous identification of the vortices. The tomography technique could be very helpful in
560 these cases, as it allows the search of dust devils events on the basis of pressure data only, clearly
561 distinguishing between events that are doubtful and highly probable.

562

563 In summary, we have shown how the tomography is a reliable method for the dust devils
564 identification and that it has a good detection efficiency. The method provides filtering,
565 separation and characterization of the dust devil signal components even in presence of strong
566 noise. For these reasons, the tomograms could be a useful tool for the detection and
567 characterisation of dust devil events for both terrestrial and Martian campaigns. The algorithm
568 can be modified by using more than one parameter in the analysis. We are working in this
569 direction, and we expect to get more accuracy in the characterization and classification of the
570 dust devils.

571

572

573 5. ACKNOWLEDGEMENTS

574

575 This work was supported by Ministerio de Economía y Competitividad of Spain (project
576 ESP2016-79135-R) and MINECO DPI 2015-65833-P. We also thank the support of Instituto de
577 Investigaciones Económicas y Sociales Francisco de Vitoria in Spain. This work was also
578 supported by the Italian Space Agency through the agreement I/018/12/0: 'DREAMS EDM
579 Payload—ExoMars 2016'.

580

581 6. REFERENCES

582

583 Aguirre, C., Serrano, E. and Pascual, P., 2013. Detection of neuronal signatures by means of
584 data-driven tomography *BMC Neuroscience*, 14 (Suppl 1), 309.

585

586 Aguirre C., Vilela Mendes R., 2014. Signal recognition and adapted filtering by non-
587 commutative tomography. *IET Signal Processing*, 8, 67-75.

588

589 Almeida, M.P., Parteli, E.J.R., Andrade, J.S., Herrmann, H.J., 2008. Giant saltation on Mars.
590 *Proc. Natl. Acad. Sci. USA* 105, 6222-6. doi: 10.1073/pnas.0800202105.

591

592 Aubry, N., Guyonnet, R., Lima, R., 1991. Spatio-temporal analysis of complex signals: Theory
593 and applications, *J. Stat. Phys.* 64, 683-739. doi: 10.1007/BF01048312.

594

595 Dente J.A., Vilela Mendes R., Lambert A. and Lima R.,1996. The bi-orthogonal decomposition
596 in image processing: Signal analysis and texture segmentation, *Signal Processing, Image*
597 *Communication* 8, 131-148.
598

599 Balme, M., Metzger, S., Towner, M., Ringrose, T., Greeley, R., & Iversen, J., 2003. Friction
600 wind speeds in dust devils: A field study. *Geophysical research letters*, 30, 16.
601

602 Balme, M., Greeley, R., 2006. Dust Devils on Earth and Mars. *Rev. Geophys.* 44, 3. doi:
603 10.1029/2005RG000188.
604

605 Briolle, F., Man'ko, V.I., Ricaud, B., Vilela Mendes, R., 2012. Non-commutative tomography:
606 a tool for data analysis and signal processing, *J. Russ. Laser Res.*, 33, 103–121.
607

608 Crozier, W.D., 1964. The electric field of a New Mexico dust devil. *J. Geophys. Res.* 69, 5427.
609 doi: 10.1029/JZ069i024p05427.
610

611 Crozier, W. D., 1970. Dust devil properties. *J. Geophys. Res.* 75, 4583–4585.
612 doi:10.1029/JC075i024p04583.
613

614 Daubechies, I., 1990. The wavelet transform: time–frequency localization and signal analysis.
615 *IEEE Trans. Inf. Theory.* 36(5), 961–1005. doi: 10.1109/18.57199.
616

617 Donoho, D.L., Stark, P.B., 1989. Uncertainty Principles and Signal Recovery, *SIAM. J. Appl.*
618 *Math.*, 49(3), 906–931. doi:10.1137/0149053.
619

620 Duff, N., Lacks, D.J., 2008. Particle dynamics simulations of triboelectric charging in granular
621 insulator systems. *Journal of Electrostatics.* 66, 51-57. doi:10.1016/j.elstat.2007.08.005.
622

623 Eden, H.F., Vonnegut, B., 1973. Electrical breakdown caused by dust motion in low pressure
624 atmospheres: Considerations for Mars. *Nature*, 280, 962–963 doi:
625 10.1126/science.180.4089.962.
626

627 Ellehoj, M.D., Gunnlaugsson, H.P., Taylor, P.A., Kahanpää, H., Bean, K.M., Cantor,
628 B.A., Gheynani, B.T., Drube, L., Fisher, D., Harri, A.M., Holstein-Rathlou, C.,
629 Lemmon, M.T., Madsen, M.B., Malin, M.C., Polkko, J., Smith, P.H., Tamppari, L.K.,
630 Weng, W., Whiteway, J., 2010. Convective vortices and dust devils at the Phoenix Mars
631 mission landing site. *J. Geophys. Res.* 115, E00E16. doi:10.1029/2009JE003413.
632

633 Esposito F., Molinaro R., Popa C. I., Molfese C., Cozzolino F., Marty L., Taj-Eddine K., Di
634 Achille G., Franzese G., Silvestro S., Ori G. G., 2016a, The role of atmospheric electric field in
635 the dust lifting process, *GRL*, 43, 5501-5508. doi: 10.1002/2016GL068463.
636

637 Esposito F., Debei, S., Bettanini, C., Molfese, C., Arruego Rodriguez, I., Colombatti, G., Harri,
638 A-M., Montmessin, F., Wilson, C., Aboudan, A., Abbaki, S., Apestigue, V., Bellucci, G.,
639 Bethelier, J-J., Brucato, J. R., Calcutt, S. B., Cortecchia, F., Cucciarrè., Di Achille, G., Ferri, F.,
640 Forget, F., Friso, E., Genzer, M., Gilbert, P., Haukka, H., Jiménez, J. J., Jiménez, S., Josset, J-
641 L., Karatekin, O., Landis, G., Lorenz, R., Manetta, M., Martinez, J., Marty, L., Mennella, V.,
642 Möhlmann, D., Moirin, D., Molinaro, R., Palomba, E., Patel, M., Pommereau, J-P., Popa, C. I.,
643 Rafkin, S., Rannou, P., Renno, N. O., Schipani, P., Schmidt, W., Segato, E., Silvestro, S., Simoes,
644 F., Simoncini, E., Spiga, A., Valero, F., Vázquez, L., Vivat, F., Witasse, O., Mugnuolo, R.,
645 Pirrotta, S., Marchetti, E., 2016b. The DREAMS experiment on board the Schiaparelli Module
646 of the ExoMars 2016 mission: design, performances and expected results, *Space Sci. Rev.*, under
647 review.
648

649 Farrell, W.M., Smith, P.H., Delory, G.T., Hillard, G.B., Marshall, J.R., Catling, D., Hecht, M.,
650 Tratt, D.M., Renno, N., Desch, M.D., Cummer, S.A., Houser, J.G., Johnson, B., 2004. Electric
651 and magnetic signatures of dust devils from the 2000-2001 MATADOR desert test, *J. Geophys.*
652 *Res.* 109 (E3). doi: 10.1029/2003JE002088.

653
654 Fenton, L., Reiss, D., Lemmon, M., Marticorena, B., Lewis, S., Cantor, B., 2016. Orbital
655 Observations of Dust Lofted by Daytime Convective Turbulence. *Space Sci. Rev.* 203, 89–142.
656

657 Fourier, J.B.J., 1888. *Théorie analytique de la Chaleur*, in Darbous, G. (Ed.): *Oeuvres de*
658 *Fourier*, (Gauthiers-Villars, Paris), Tome premie.

659
660 Franzese G., Esposito F., Lorenz R., Silvestro S., Popa C., Molinaro R., Cozzolino F., Molfese
661 C., Marty L., Deniskina N., 2017. Electric properties of dust devils, *Earth and Planetary science*
662 *letter*, under review

663
664 Freier, G.D., 1960. The electric field of a large dust devil. *J. Geophys. Res.* 65(10), 3504
665 doi:10.1029/JZ065i010p03504.

666
667 Gimenez-Bravo A., Aguirre C., Vázquez, L., 2013. Tomographic Signal Analysis for the
668 Detection of Dust-Devils in Mars Atmosphere, The Fourth Moscow Solar System Symposium
(4M-S3) IKI RAS, 14-18 October.

669
670 Greeley, R., 2002. Saltation impact as a means for raising dust on Mars. *Planetary and Space*
671 *Science*, 50 (2), 151-155.

672
673 Greeley, R., Balme, M. R., Iversen, J. D., Metzger, S., Mickelson, R., Phoreman, J., White, B.,
674 2003. Martian dust devils: Laboratory simulations of particle threshold. *Journal of Geophysical*
675 *Research: Planets*, 108 (E5).

676
677 Harrison R.G., Barth, E., Esposito, F., Merrison, J., Montmessin, F., Aplin, K.L., Borlina, C.,
678 Berthelier, J.J., Déprez, G., Farrell, W.M., Houghton, I.M.P., Renno, N.O., Nicoll, K.A.,
679 Tripathi, S.N., Zimmerman, M., 2016. Applications of Electrified Dust and Dust Devil
680 Electrodynamics to Martian Atmospheric Electricity, *Space Sci Rev.* doi: 10.1007/s11214-016-
681 0241-8.

682
683 Husimi, K., 1940. Some formal properties of the density matrix. *Proc. Phys. Mat. Soc. Jpn.* 22,
684 264–314. Inculet, I.I., Peter Castle, G.S., Aartsen, G., 2006. Generation of bipolar electric fields
685 during industrial handling of powders. *Chem. Eng. Sci.* 61, 7 doi:10.1016/j.ces.2005.05.005.
686

687
688 Iversen, J. D., White, B. R. 1982, Saltation threshold on Earth, Mars and Venus. *Sedimentology*,
689 29, 111–119. doi:10.1111/j.1365-3091.1982.tb01713.x.

690
691 Jackson, B., Lorenz, R., 2015. A multiyear dust devil vortex survey using an automated search
692 of pressure time series. *J. Geophys. Res. Planets.* 120, 3, 401-412. doi:10.1002/2014JE004712.

693
694 Kano, Y., 1965. A new phase-space distribution function in the statistical theory of the
695 electromagnetic field. *J. Math. Phys.* 6, 1913–1915.

696
697 Klose, M., Jemmett-Smith, B.C., Kahanpää, H., Kahre, M., Knippertz, P., Lemmon, M.T.,
698 Lewis, S.R., Lorenz, R.D., Neakrase, L.D. V., Newman, C., Patel, M.R., Reiss, D., 2016. Dust
699 devil sediment transport: From lab to field to global impact. *Space Sci. Rev.* 203, 377–426.

700 Kok, J.F., Renno, N.O., 2009. A comprehensive numerical model of steady-state saltation
701 (COMSALT), *J. Geophys. Res.* 114, D17204. doi: 10.1029/2009JD011702.
702

703 Kok, J. F., 2010. Difference in the Wind Speeds Required for Initiation versus Continuation of
704 Sand Transport on Mars: Implications for Dunes and Dust Storms. *Phys. Rev. Lett.* 104 074502
705 doi: 10.1103/PhysRevLett.104.074502).
706

707 Lorenz, R. D., Jackson, B. K., 2016. Dust devil populations and statistics. *Space Science*
708 *Reviews*, 203(1-4), 277-297.
709

710 Lorenz, R. D., 2016. Heuristic estimation of dust devil vortex parameters and trajectories from
711 single-station meteorological observations: Application to InSight at Mars. *Icarus*, 271, 326-
712 337.
713

714 Lumley, J. L., Panofsky, H. A., 1964. The structure of atmospheric turbulence.
715

716 Man'ko, V.I., Vilela Mendes, R., 1999. Noncommutative time–frequency tomography', *Phys.*
717 *Lett. A*, 263, 53–59.
718

719 Man'ko M.A., Man'ko V.I., and Vilela Mendes R., 2001. Tomograms and other transforms: A
720 unified view. *J. Physics A: Math. and Gen.* 34, 8321.
721

722 Murphy J., Steakley, K., Balme, M., Deprez, G., Esposito, F., Kahanpää, H., Lemmon, M.,
723 Lorenz, R., Murdoch, N., Neakrase, L., Patel, M., Whelley, P., 2016. Field Measurements of
724 Terrestrial and Martian Dust Devils, *Space Sci Rev.* doi: 10.1007/s11214-016-0283-y.
725

726 Neakrase, L. D., Greeley, R., 2010a. Dust devil sediment flux on Earth and Mars: Laboratory
727 simulations. *Icarus*, 206(1), 306-318.
728

729 Neakrase, L. D., Greeley, R., 2010b. Dust devils in the laboratory: Effect of surface roughness
730 on vortex dynamics. *Journal of Geophysical Research: Planets*, 115(E5).
731

732 Neakrase L. D. V., Balme, M. R., Esposito, F., Kelling, T., Klose, M., Kok, J. F., Marticorena,
733 B., Merrison, J., Patel, M., Wurm, G., 2016. Particle Lifting Processes in Dust Devils. *Space Sci*
734 *Rev.* doi:10.1007/s11214-016-0296-6.

735

736 Neubauer, F.M., 1966. Thermal convection in the Martian atmosphere. *J. Geophys. Res.* 71,
737 2419–2426. doi: 10.1029/JZ071i010p02419.
738

739 Ringrose, T.J., Towner, M.C., Zarnecki, J.C., 2003. Convective vortices on Mars: are-analysis
740 of Viking Lander 2 meteorological data, sols 1-60. *Icarus* 163, 1, 78–87. doi: 10.1016/S0019-
741 1035(03)00073-3.
742

743 Toigo, A.D., Richardson, M.I., Ewald, S.P., Gierasch, P.J., 2003. Numerical simulation of
744 Martian dust devils. *J. Geophys. Res.* 108, E6, 5047. doi:10.1029/2002JE002002.
745

746 Thomas, P.C., Gierasch, P.J., 1985. Dust devils on Mars, *Science*, 230, 175–177 doi:
747 10.1126/science.230.4722.175.
748

749 Ville, J., 1948. Théorie et applications de la notion de signal analytique. *Cables Transm.* 2 A.
750 61–74.

751
752 Wigner, E., 1932. On the quantum correction for thermodynamic equilibrium. *Phys. Rev.* 40,
753 749–759.
754
755 Zhai, Y., Cummer, S.A., Farrell, W.M., 2006. Quasi-electrostatic field analysis and simulation
756 of martian and terrestrial dust devils. *J. Geophys. Res* 111 (E6). doi: 10.1029/2005JE002618.
757
758
759